Phonon stability boundary and deep elastic strain engineering of lattice thermal conductivity

Zhe Shi[a,*], Evgenii Tsymbalov[b,*], Wencong Shi[c], Ariel Barr[a], Qingjie Li[a], Jiangxu Li[d], Xing-Qiu Chen[d], Ming Dao[e], Subra Suresh[c,e,⊥], and Ju Li[a,e⊥]

[a] Department of Nuclear Science and Engineering, Massachusetts Institute of Technology, Cambridge, Massachusetts 02139, USA
[b] Independent Researcher, Aachen, North Rhine-Westphalia 52070, Germany
[c] Department of Mechanical Engineering, Nanyang Technological University, Singapore 639798, Republic of Singapore
[d] Shenyang National Laboratory for Materials Science, Institute of Metal Research, Chinese Academy of Sciences, Shenyang, China
[e] Department of Materials Science and Engineering, Massachusetts Institute of Technology, Cambridge, Massachusetts 02139, USA

* These authors contributed equally to this work.
⊥To whom correspondence may be addressed. Email: ssuresh@mit.edu or liju@mit.edu.

Abstract

Recent studies have reported the experimental discovery that nanoscale specimens of even a natural material, such as diamond, can be deformed elastically to as much as 10% tensile elastic strain at room temperature without the onset of permanent damage or fracture. Computational work combining *ab initio* calculations and machine learning algorithms has further demonstrated that the bandgap of diamond can be altered significantly purely by reversible elastic straining. These findings open up unprecedented possibilities for designing materials and devices with extreme physical properties and performance characteristics for a variety of technological applications. However, a general scientific framework to guide the design of engineering materials through such elastic strain engineering has not yet been developed. By combining first-principles calculations with machine learning, we present here a general approach to map out the entire phonon stability boundary in six-dimensional strain space, which can guide the elastic strain engineering (ESE) of a material without phase transitions. We focus on ESE of vibrational properties, including harmonic phonon dispersions, nonlinear phonon scattering and thermal conductivity. Whereas the framework presented here can be applied to any material, we show as an example demonstration that the room-temperature lattice thermal conductivity of diamond can be increased by more than 100% or reduced by more than 95% purely by ESE, without triggering phonon instabilities. Such a framework opens the door for tailoring of thermal-barrier,

thermoelectric, and electro-optical properties of materials and devices through the purposeful design of homogeneous or inhomogeneous strains.

Keywords

Phonon stability boundary; Thermal conductivity; Elastic strain engineering; Machine learning; First-principles simulation

Significance statement

Vibrational properties, such as phonon dispersion and scattering, play a crucial role in a material's mechanical, thermal, and thermoelectric behavior. Knowledge of the phonon stability boundary in the full strain tensor space, which gives the upper limit of elastic strain engineering (ESE), is essential for engineering the electronic and thermal properties solely through strains. Here *ab initio* calculations and machine learning are combined to develop a general framework that reveals the phonon stability boundary in six-dimensional strain space. It is shown that the lattice thermal conductivity of diamond can be increased by more than 100% or reduced by more than 95% purely by reversible elastic strain without the onset of phonon instabilities.

Introduction

The fundamental characteristics of semiconductors, such as electrical and thermal transport properties, can be modified through the controlled introduction of elastic strain[1–3]. With an ever-accelerating search for improved electrical and thermal characteristics of devices, tuning phonon properties through mechanical strains offers a powerful pathway to enhance the performance of microelectronic and optoelectronic devices. Just as the properties of silicon can be spatially tuned on the same single-crystalline wafer by variable-concentration chemical doping[4], it is also possible to envision the tailoring of physical properties through the rational design of inhomogeneous elastic strain distribution to achieve variable bandgap[5], carrier mobility[6], and thermal barrier properties on the same chip. In this work, we consider elastic strains that are an order of magnitude larger than those hitherto adopted by the semiconductor industry, which typically involve strains on the order of one percent[7–9].

There exists an ideal strain limit ($\boldsymbol{\varepsilon}_{\mathrm{ideal}}$), which is the theoretical upper bound for reversible elastic deformation for a perfect crystal at the absolute zero temperature. Beyond $\boldsymbol{\varepsilon}_{\mathrm{ideal}}$, the onset of relaxation by phonon instability at either $\mathbf{k} = \mathbf{0}$ (Γ point) or finite-$\mathbf{k}$ would occur, which would inevitably lead to fracture, plasticity, or phase transition[10]. In actual experiments, both zero-temperature and defect-free conditions are impractical, and the fact that every real material must have a surface, which is a defect, already renders $\boldsymbol{\varepsilon}_{\mathrm{ideal}}$ unattainable. By including the effects of temperature, microstructure, and defects present in materials, the more conservative $\boldsymbol{\varepsilon}_{\mathrm{real}}$ boundary may be found, and the six-dimensional (6D) strain space circumscribed by the five-dimensional (5D) $\boldsymbol{\varepsilon}_{\mathrm{real}}$ boundary is a subset of that by $\boldsymbol{\varepsilon}_{\mathrm{ideal}}$.

A large dynamic range for $\boldsymbol{\varepsilon}_{\mathrm{real}}$ has been discovered in recent studies in nano-scale materials at room temperature without the onset of plasticity, phase transformation, or fracture for time periods long enough for applications. Even for the hardest natural crystalline diamond, mechanical bending experiments involving single crystal nanoscale needles have shown[11] that local elastic tensile strains of nearly 10% can be achieved prior to the onset of fracture, whereas nanoscale polycrystalline diamond could be elastically strained to nearly 4%. Similar magnitudes of elastic strains have subsequently been demonstrated in both synthetic and natural diamonds in the form of nanoneedles and nanowires[12,13], and micro-bridged arrays[13]. This is possible at the nanoscale, where small characteristic dimensions and low defect populations in pure diamond make it possible to approach $\boldsymbol{\varepsilon}_{\mathrm{ideal}}$ during mechanical deformation[2]. Silicon in the nanowire form can withstand 15% uniaxial tension without the onset of plasticity[15], which is more than one order of magnitude higher than that currently employed by the semiconductor industry for its strained silicon technology. The realization of ultra-large elastic deformation in nanoscale dimensions of semiconductor materials, together with the ultra-large levels of thermal conductivity in certain semiconductors such as diamond, has created opportunities for the custom design of performance characteristics through elastic strain engineering (ESE). These provide pathways to realizing a dynamic and broad range of physical properties, i.e. from electronic insulator to conductor[16], or

from thermal conductor to thermal barrier, which may be achieved on the same single crystal by varying the spatial distribution of strain[17].

In this work we focus on the upper bound of theoretical strain, $\boldsymbol{\varepsilon}_{\text{ideal}}$, which envelops the practically attainable $\boldsymbol{\varepsilon}_{\text{real}}$ boundary. The mapping of the $\boldsymbol{\varepsilon}_{\text{ideal}}$ hypersurface necessitates an evaluation of phonon stability within the six-dimensional (6D) strain space represented by the elastic strain tensor $\boldsymbol{\varepsilon} \equiv (\varepsilon_{11}, \varepsilon_{22}, \varepsilon_{33}, \varepsilon_{23}, \varepsilon_{13}, \varepsilon_{12})$. In the low-temperature and defect-free limit, the mechanical stability of the crystal is preserved so long as the frequency ω of each phonon mode ν is real (non-imaginary) for all wave vectors $\mathbf{k}$ throughout the Brillouin zone. If this condition is violated, energy reduction can be achieved by following the eigenvector of the unstable phonon (in unit cell if Γ-point soft phonon, and in an enlarged supercell if finite-$\mathbf{k}$ soft phonon), a barrierless relaxation that can happen even at $T = 0$ K. $\boldsymbol{\varepsilon}_{\text{ideal}}$ can thus be regarded as a strain hypersurface in 6D that corresponds to the onset of non-real phonon frequencies for arbitrary $\mathbf{k}$ and ν. Ordinarily, computation of phonon properties directly comparable with experimental data from neutron or X-ray inelastic scattering requires first-principles calculations based on the finite displacement method or density functional perturbation theory (DFPT)[18]. To outline the intractable computational burden of this task, consider the phonon band structure $\omega_\nu(\boldsymbol{\varepsilon}; \mathbf{k})$, which is a function of wave vector $\mathbf{k}$ and crystal strain $\boldsymbol{\varepsilon}$ where $\mathbf{k} \in \mathbb{C}^3$, $\boldsymbol{\varepsilon} \in \mathbb{R}^6$, with 9 dependent variables (10 when including the discrete phonon branch index ν), for an arbitrary bulk semiconductor crystal. Mapping the phonon band frequency space with a tabulation approach would then entail many millions of first-principles calculations, with additional computational costs incurred to include ESE effects on lattice thermal conductivity.

To overcome these difficulties, we present a general method that combines machine learning (ML) and *ab initio* calculations to identify the theoretical ESE upper bound that defines the phonon stability boundary and $\boldsymbol{\varepsilon}_{\text{ideal}}$. This method invokes artificial neural networks (NNs) to predict, within a reasonable degree of accuracy, material properties as a function of strain while utilizing minimally required input data. In analogy with the yield surface commonly used to describe plastic deformation of metallic materials, we visualize the phonon stability boundary of a bulk semiconductor crystal in the elastic strain $\boldsymbol{\varepsilon}_{\text{ideal}}$ or stress space. We demonstrate the potential of our method for engineering phonon band structure, phonon density of states (DOS), and thermal transport properties. Exemplifying the potential for semiconductor performance optimization afforded by our method, we demonstrate that the lattice thermal conductivity of diamond can span from sub-100 $\text{W}\cdot\text{m}^{-1}\cdot\text{K}^{-1}$ up to 6000 $\text{W}\cdot\text{m}^{-1}\cdot\text{K}^{-1}$ solely through mechanical strain. The general method developed in this work, with specific demonstrations of its application for the case of diamond, is thus seen to provide a broad framework to guide elastic strain engineering of materials to tailor their physical properties, such as phonon band structure and thermal conductivity.

Results

1. Machine-learning phonon band structure and DOS

ML methods have become indispensable for solving problems with extensive parameter spaces that are challenging to tackle through conventional analytical or numerical means. In the domain of our concern, this challenge manifests prominently in the modeling of phonon dispersion as a function of strain tensor. To address this, the present work employs two ML models: a feed-forward neural network (FNN) and a convolutional neural network (CNN). In the study of electronic properties, FNNs have been demonstrated to provide high accuracy for single-value regression tasks, such as predicting the scalar-valued electronic bandgap[5]. By contrast, drawing an analogy between dispersion relations and RGB pixel color encoding of digital images, CNN can be chosen as a base architecture to fit band structure. CNNs were found to excel at learning multiple energy bands simultaneously with the inclusion of "intra/inter-band correlation", and to achieve state-of-the-art band curvature accuracy[6].

Two generic NN training processes to learn strain-dependent phonon-related properties are shown in Figure 1. Both processes take the elastic strain state $\boldsymbol{\varepsilon}$ as input to learn phonon dispersion and DOS $g(\boldsymbol{\varepsilon}; \omega)$. In contrast to the FNN method employed for learning 6 bands (3 acoustic and 3 optical) separately, a CNN method applies 3D convolution in reciprocal space and learns the band structure $\omega_\nu(\boldsymbol{\varepsilon}; \mathbf{k})$ in its entirety. Similarly, CNN applies 1D convolution in the frequency domain to learn the DOS, which is not feasible in the FNN model. The phonon stability can either be directly machine-learned as a classification task (indicated by the orange arrow in Figure 1a) or predicted by postprocessing the as-trained phonon DOS or band structure FNN/CNN models. The results yielded from learning ~15,000 strain data for the phonon stability boundary, band structure, and DOS in the general 6D strain space and two 3D subspaces are summarized in Table 1. A detailed description of first-principles data acquisition and the NN architecture can be found in the Method section.

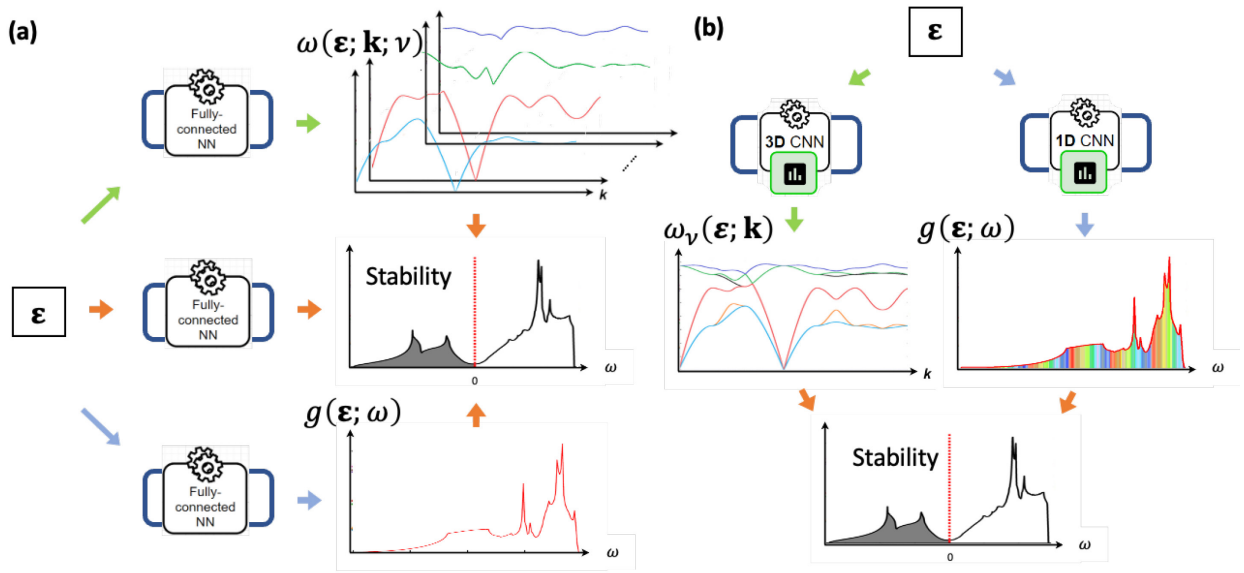

Figure 1. ML workflow for phonon-related properties with strain information used as input. When adopting (a) FNN models, the phonon stability can either be learned by directly fitting the onset of imaginary frequencies or analyzed from ML-predicted phonon band structure or DOS. The band structure, $\omega(\boldsymbol{\varepsilon}; \mathbf{k}; \nu)$,

is treated as 6 separate bands. When (b) CNN models are used, the direct ML target can be band structure or DOS. The band structure, $\omega_\nu(\boldsymbol{\varepsilon};\mathbf{k})$, is learned as a whole. The green, blue and orange arrows indicate the procedural steps for learning band structure, DOS, and phonon stability, respectively.

Table 1. Summary of the ML accuracies reached for phonon stability boundary, DOS, and band structure corresponding to strain states in the $\varepsilon_{11}-\varepsilon_{22}-\varepsilon_{33}$ normal strain space, the $\varepsilon_{23}-\varepsilon_{13}-\varepsilon_{12}$ shear strain space, and general 6D hyperspace. The DOS results are expressed in mean absolute error (MAE). The band structure results are given by a relative error range due to band dependence.

ML target	$\varepsilon_{11}-\varepsilon_{22}-\varepsilon_{33}$ normal strain space	$\varepsilon_{23}-\varepsilon_{13}-\varepsilon_{12}$ shear strain space	General 6D strain space
Stability boundary	97%	95%	94%
DOS	0.009	0.01	0.02
Band structure	1.1-2.5%	3.3-4.6%	4-4.5%

2. Analysis of the phonon stability boundary

The 6D strain space consists of mixed deformation states that combine standard hydrostatic, uniaxial, and pure shear strains. Visualization of this space is important as it allows for the delineation of the phonon stability boundary, defining an upper bound for the "safe" working limit of applied strains.

We trained ML models to reveal the stability boundaries in two 3D subspaces by constraining three of the six strain components. Figures 2a and 2b demonstrate the stability boundary in pure compressive and tensile strain subspace ($\varepsilon_{23} = \varepsilon_{13} = \varepsilon_{12} = 0$). Figures 2c and 2d show the stability boundary in the shear strain subspace ($\varepsilon_{11} = \varepsilon_{22} = \varepsilon_{33} = 0$). Similar to the isosurfaces used to assess the boundaries of bandgap modulation by recourse to ESE in our previous work[5,6], the present study deals with phonon stability boundary signifying the onset of imaginary phonon frequencies for a given strain state on the stability boundary at critical wave vectors $\mathbf{k_c}$.

In general, there are three types of the critical wave vector in the strain spaces considered. Following the notation rules introduced in *SI Appendix, Notation*, they can be classified as:

- The Γ type: $\mathbf{k_c} = (0, 0, 0)$
- The 'Δ' type: $\mathbf{k_c} = (\xi, \xi, 0)$, $(\xi, 0, \xi)$ or $(0, \xi, \xi)$, where $0 < \xi < 0.5$
- The 'L' type: $\mathbf{k_c} = (0, 0, 0.5)$, $(0, 0.5, 0)$ or $(0.5, 0, 0)$

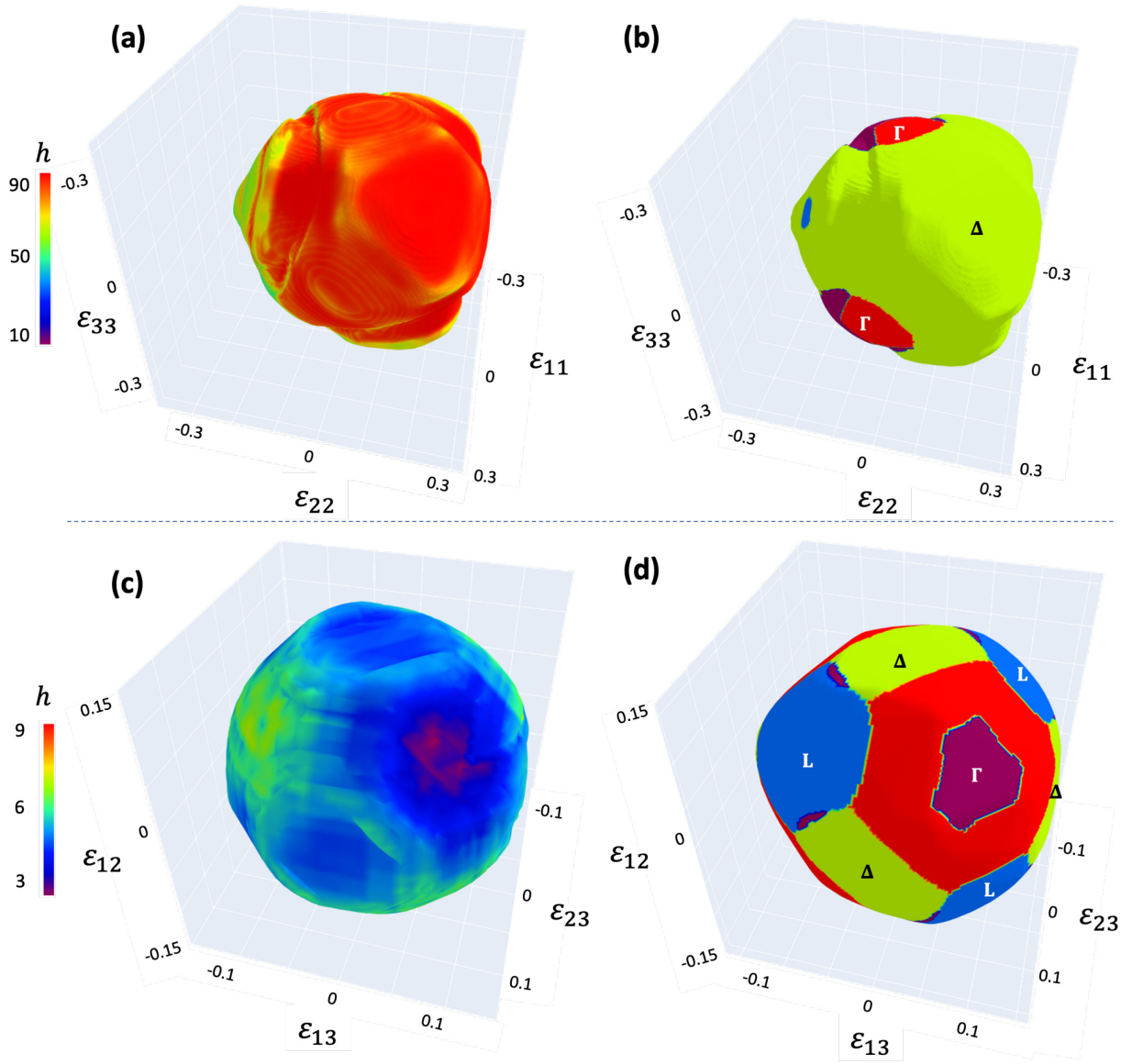

Figure 2. 3D phonon stability boundaries. The stability boundaries for the $\varepsilon_{11}-\varepsilon_{22}-\varepsilon_{33}$ normal strain subspace colored by (a) the elastic strain energy density h (unit: meV/Å^3) and partitioned by (b) critical wave vector $\mathbf{k}_c$. The stability boundaries for the $\varepsilon_{23}-\varepsilon_{13}-\varepsilon_{12}$ shear strain subspace colored by (c) h and partitioned by (d) $\mathbf{k}_c$. The regions in light green, blue, red/crimson correspond to $\mathbf{k}_c$ of the 'Δ', 'L', 'Γ' types, respectively.

In Figure 3, the general phonon stability boundary, a 5D surface denoted as $f(\varepsilon_{11},\varepsilon_{22},\varepsilon_{33},\varepsilon_{23},\varepsilon_{13},\varepsilon_{12})=0$, can be partially visualized through pair-plot slices of the 6D space. The six pairwise-normal-strain subfigures in the top left corner can be thought of as origin-crossing vertical or horizontal cuts of the 3D volume in Figure 2a or 2b, while the six pairwise-shear-strain subfigures in the lower right corner can be thought of as origin-crossing vertical or horizontal cuts of the 3D volume in Figure 2c or 2d. Crystal deformation symmetries were enforced

when learning the stability boundary through ML models. When the strain state is composed of a single strain type (either normal-normal or shear-shear), the stability boundary has higher symmetry. The normal-normal strain stability boundaries on the top 3 × 3 left corner are phonon boundary surfaces with *2mm* symmetry, the shear-shear stability boundaries on the lower 3 × 3 right corner are quatrefoils with *4mm* symmetry, while all other mixed strain states such as the $\varepsilon_{12}-\varepsilon_{33}$ normal-shear pair have only *m* symmetry with a "fish cracker" shaped stability boundaries. Overall, structural instability is more easily initiated by shear strain than normal strain, as indicated by the reduced shear strain axial extent and commensurate volume reduction.

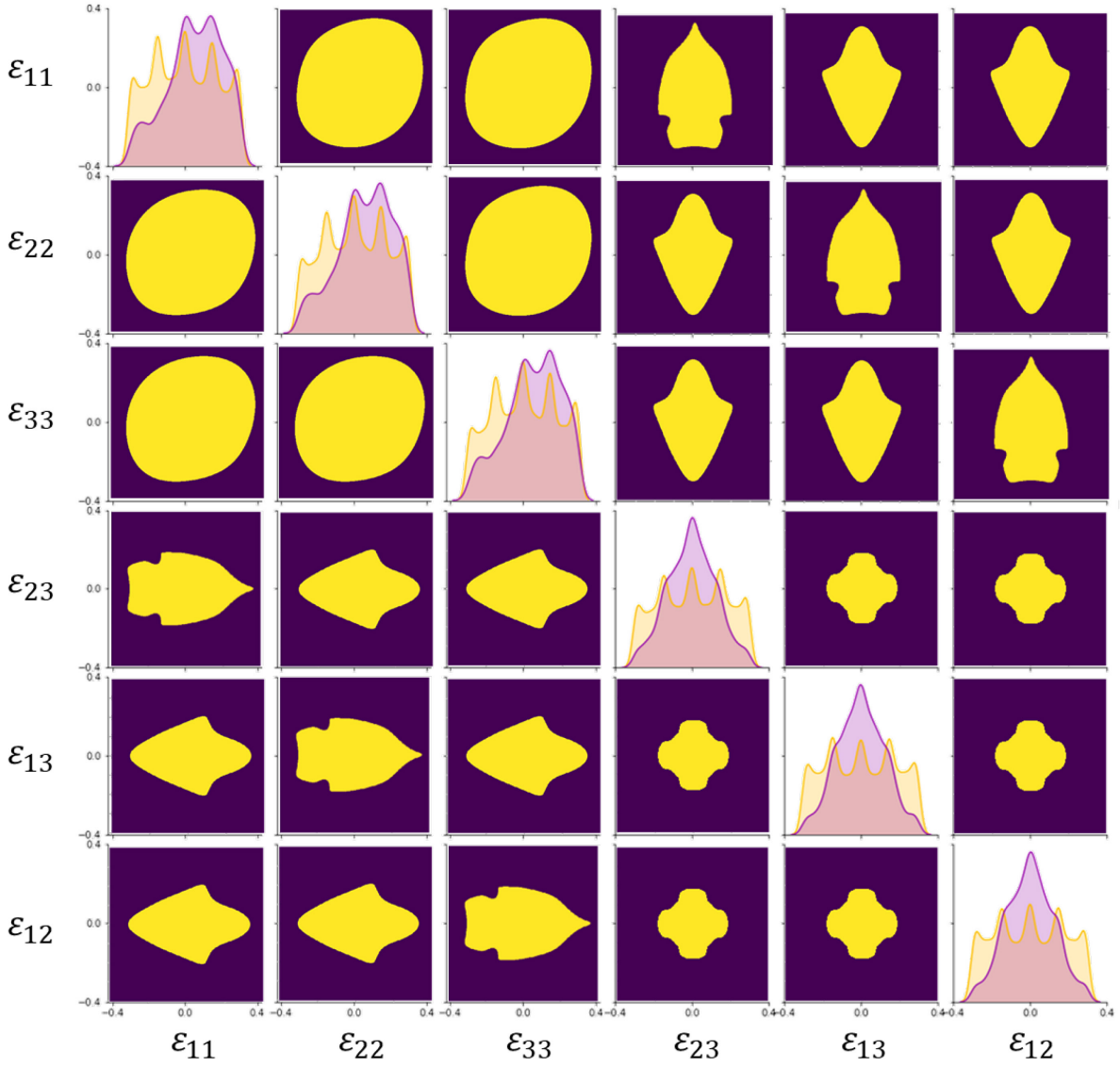

Figure 3. Phonon stability boundary pair-plots. The subfigures are 2D cuts of the 6D strain space with the remaining 4 strain components fixed at zero. For instance, strains in the $\varepsilon_{11}\varepsilon_{12}$ subfigure in the lowest-left corner have $\varepsilon_{22} = \varepsilon_{33} = \varepsilon_{23} = \varepsilon_{13} = 0$. The diagonal subfigures are histograms for strain states spanning -0.4 to 0.4. Due to the symmetry in strain space, the 15 subfigures in the upper triangular region have a one-to-one correspondence with the 15 subfigures in the lower triangular region at relative positions.

3. Deep ESE of lattice thermal conductivity

The thermodynamic and thermal transport properties of a solid due to lattice dynamics are directly related to its phonon characteristics. By far, the largest contribution to thermal conductivity $\boldsymbol{\kappa}$ of dielectric solids comes from the lattice thermal conductivity $\boldsymbol{\kappa}_l$, which arises from the combined contribution of all phonon modes (with the dominant ones being acoustic). ML techniques developed for providing $\boldsymbol{\kappa}_l$ of undeformed solids such as Si, MgO and $LiCoO_2$ made possible an reduction of the computational costs associated with high-order phonon scattering analysis[19,20]. Strain engineering of phononics[21] is of interest in fields such as thermoelectricity, where achieving low $\boldsymbol{\kappa}$ is sought in order to increase the figure of merit for a thermoelectric material. In industrial applications where thermal insulation is important, materials with low $\boldsymbol{\kappa}$ values are used for thermal barrier coatings[22]. In electronic device applications, materials with high $\boldsymbol{\kappa}$ values are preferred in order to prevent damage from heat accumulation[23,24], while it may be preferable to seek low $\boldsymbol{\kappa}$ values in some regions for thermal insulation purposes (from the hot regions) as well. Effective control of $\boldsymbol{\kappa}_l$ through ESE therefore has potential technological applications.

For an ML method to accurately acquire the strain dependence of $\boldsymbol{\kappa}_l$ within the 6D strain space, it is necessary to accumulate a sufficiently large collection of $\boldsymbol{\kappa}_l$ values under different strain states to use as a training dataset. Recent advancements in the field have shown the feasibility of training NNs[25] to solve the phonon Peierls-Boltzmann transport equation (BTE). For enhanced accuracy in our study, we rely on the first-principles approach for solving the phonon BTE to determine $\boldsymbol{\kappa}_l$. High-throughput computations on ~10,000 strain states that are randomly distributed in the 6D space were performed to build the training dataset. Additional computational details are included in the Method section, with specifics on $\boldsymbol{\kappa}_l$ given in *SI Appendix, Theoretical background of* $\boldsymbol{\kappa}_l$.

The average lattice thermal conductivity $\overline{\kappa}_l(\boldsymbol{\varepsilon})$ and the elastic strain energy density $h(\boldsymbol{\varepsilon})$ as functions of strain tensor $\boldsymbol{\varepsilon}$ within the 6D strain space were obtained using the ML model, as shown in Figure 4a. The values of scalar $\overline{\kappa}_l$ are obtained by taking the average of the three $\boldsymbol{\kappa}_l$ tensor eigenvalues, $\overline{\kappa}_l \equiv \frac{\mathrm{Tr}(\boldsymbol{\kappa}_l)}{3}$. The distribution of possible $\overline{\kappa}_l$ is indicated in Figure 4a by purple shading, with darker tonal values indicating that a larger number of strain states are able to achieve a specific $\overline{\kappa}_l$ value for a given h, where h denotes the elastic strain energy density in the unit of meV/Å^3. The cumulative "density of states" of average thermal conductivity $c(\overline{\kappa}_l'; h')$ is defined as

$$c(\overline{\kappa}_l'; h') \equiv \int_{h(\boldsymbol{\varepsilon})<h'} d^6\boldsymbol{\varepsilon}\,\delta\big(\overline{\kappa}_l' - \overline{\kappa}_l(\boldsymbol{\varepsilon})\big) = \int d^6\boldsymbol{\varepsilon}\,\delta\big(\overline{\kappa}_l' - \overline{\kappa}_l(\boldsymbol{\varepsilon})\big)\Theta\big(h' - h(\boldsymbol{\varepsilon})\big) \qquad (1)$$

where $\delta(\cdot)$ and $\Theta(\cdot)$ are the Dirac delta and Heaviside step functions, respectively, and $d^6\boldsymbol{\varepsilon} \equiv d\varepsilon_{11}d\varepsilon_{22}d\varepsilon_{33}d\varepsilon_{23}d\varepsilon_{13}d\varepsilon_{12} \in \mathbb{R}^6$ is a volume element of the 6D strain space. The joint density of states of $\overline{\kappa}_l$ at h' can then be expressed as

$$g(\bar{\kappa}_l{}';h') \equiv \frac{\partial c(\bar{\kappa}_l{}';h')}{\partial h'} = \int d^6\boldsymbol{\varepsilon}\delta\big(\bar{\kappa}_l{}' - \bar{\kappa}_l(\boldsymbol{\varepsilon})\big)\delta\big(h' - h(\boldsymbol{\varepsilon})\big) \quad (2)$$

g is found by considering all possible strain states and the resultant distribution of $\bar{\kappa}_l$ arising from these states in the elastic strain energy density interval of $(h - \frac{dh}{2}, h + \frac{dh}{2})$. The function $g(\bar{\kappa}_l{}';h')$ provides information for finding accessible thermal conductivity values at different energy costs. A lower and upper envelope function rendered as the purple dashed and solid lines in Figure 4a can also be defined based on g, respectively:

$$\bar{\kappa}_l{}^{\text{lower}}(h) \equiv \inf_{\bar{\kappa}_l}\big(g(\bar{\kappa}_l;h)\big), \qquad \bar{\kappa}_l{}^{\text{upper}}(h) \equiv \sup_{\bar{\kappa}_l}\big(g(\bar{\kappa}_l;h)\big) \quad (3)$$

By tracing $\bar{\kappa}_l{}^{\text{lower}}$ and $\bar{\kappa}_l{}^{\text{upper}}$ in Figure 4a, it is found that diamond, as the best thermal conductor present in nature, can have its lattice thermal conductivity either doubled, or shrunk to sub-100 $\text{W}\cdot\text{m}^{-1}\cdot\text{K}^{-1}$ (i.e. decreasing by more than 95%), purely through reversible elastic strain. These changes point to a very broad dynamic range in thermal transport properties as the strain tensor is varied, while still staying in the potential energy basin of the diamond phase without any phase transitions. What can also be deduced from Figure 4a is that the lower bound guides the strain pathway, with the least elastic strain energy density (or "energy expenditure") to realize a target figure of merit (e.g., a lower thermal conductivity, if it is desirable to make a thermal barrier out of diamond, which is typically a good thermal conductor). Thus, the $\bar{\kappa}_l{}^{\text{lower}}(h)$ function could be used as a blueprint for designing thermal barrier structures with minimal strain energy density.

To assess the structural robustness of deformed diamond in 6D, one can define a "phonon softness" term by considering the integration of ω_ν^2 over the Brillouin zone for each phonon branch ν:

$$s \equiv \sum_\nu \int_{\text{BZ}} \omega_\nu^2 d\mathbf{k} \quad (4)$$

There exist other definitions of s as well, details of which can be found in Table S1 and Figure S1; these different possibilities provide essentially similar results. Relative softness can then be defined as the ratio between softness in deformed and undeformed states:

$$s_r(\boldsymbol{\varepsilon}) \equiv \frac{s(\boldsymbol{\varepsilon})}{s(\boldsymbol{\varepsilon} = \mathbf{0})} \quad (5)$$

In general, deformation causes the thermal conductivity to decrease, as indicated by the color scheme for s_r in Figure 4b. This trend can be more easily seen in Figure 4c, where the plot of s_r against $\bar{\kappa}_l$ is obtained from the projection of the data in the s_r-$\bar{\kappa}_l$-h parameter space. As phonon frequencies get smaller when $s_r(\boldsymbol{\varepsilon}) < 1$, larger wavevector phonons become dominant, and 3-phonon scattering processes are more likely. When such processes occur, the sum of two phonon wavevectors may exceed the first Brillouin zone, leading to Umklapp phonon-phonon scattering,

where $\mathbf{k}_1+\mathbf{k}_2-\mathbf{k}_3$ (net combination of the incoming and outgoing phonon wavevectors involved in the nonlinear scattering) is a non-zero reciprocal vector of the host crystal. As seen in the cyan color projection in Figure 4c, this generally results in smaller thermal conductivity. The brown projection in Figure 4c corresponds to the relation between $s_r(\boldsymbol{\varepsilon})$ and h, which is not a bijective trend. There are instances where $s_r(\boldsymbol{\varepsilon}) < 1$ and $s_r(\boldsymbol{\varepsilon}) > 1$ for the same elastic strain energy density h, as the same h can correspond to different strain states, e.g., compressive and tensile deformations bearing the same elastic energy tend to have different effects on s_r.

To evaluate the stability of a given strain state $\boldsymbol{\varepsilon}$, we define the smallest possible Euclidean distance from $\boldsymbol{\varepsilon}$ to the $\boldsymbol{\varepsilon}_{\text{ideal}}$ stability boundary hypersurface as $d_{\text{m}}(\boldsymbol{\varepsilon})$, with a strain-space distance metric of

$$d \equiv \sqrt{(\varepsilon_{11}-\tilde{\varepsilon}_{11})^2+(\varepsilon_{22}-\tilde{\varepsilon}_{22})^2+(\varepsilon_{33}-\tilde{\varepsilon}_{33})^2+2(\varepsilon_{23}-\tilde{\varepsilon}_{23})^2+2(\varepsilon_{13}-\tilde{\varepsilon}_{13})^2+2(\varepsilon_{12}-\tilde{\varepsilon}_{12})^2} \quad (6)$$

between any two strain tensors $\boldsymbol{\varepsilon}$ and $\tilde{\boldsymbol{\varepsilon}}$, and $d_{\text{m}}(\boldsymbol{\varepsilon})$ is the minimum of all d's connecting $\boldsymbol{\varepsilon}$ to a point on the surface. The bigger the d_{m} value, the farther it is from losing stability. The relation among d_{m}, h, and $\overline{\kappa_l}$ is illustrated in Figure 4d. In the blue projection, d_{m} is plotted against $\overline{\kappa_l}$. It shows that a given $\overline{\kappa_l}$ value can correspond to a range of different d_{m} values. Thus, to modulate thermal conductivity through ESE, one could always choose the strain states that have a relatively large d_{m} value to achieve a targeted $\overline{\kappa_l}$ through elastic deformation with higher safety factors. The green projection in Figure 4d is the d_{m} vs h relation, which shows an increase in h is usually accompanied by a reduction of d_{m}, i.e., with more strain energy stored in a material, it is more likely to lose phonon stability.

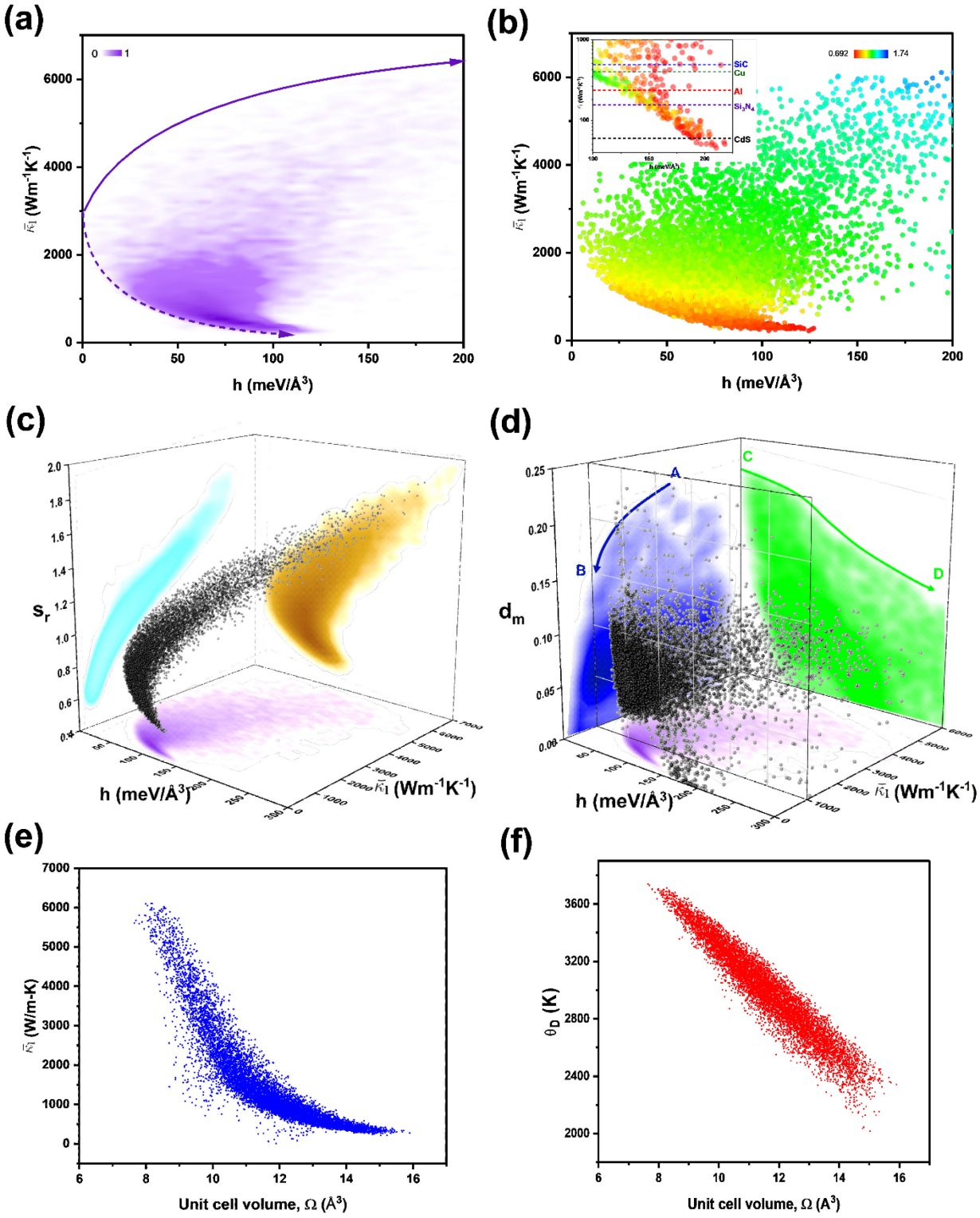

Figure 4. Deep ESE of thermal conductivity. (a) Distribution of average lattice thermal conductivity ($\overline{\kappa_l}$) over different elastic strain energy density (h) values. Darker tonal values indicate that a larger number of strain states within the sampled strain space are able to achieve a specific $\overline{\kappa_l}$ value at a given h. (b) Scatter plot of $\overline{\kappa_l}$ and h. The color spectrum denotes relative softness values. Inset is a zoomed-in logscale plot of

the small $\bar{\kappa}_l$ region, in comparison with other well-known components used in the electronics industry. (c) Cross plots of h, $\bar{\kappa}_l$, and relative softness in 3D. (d) A plot of h, $\bar{\kappa}_l$, and distance to the stability boundary d_m. The $d_\mathrm{m} - h$ and $d_\mathrm{m} - \bar{\kappa}_l$ relations are illustrated by the 2D projections in green and blue, respectively. Note that the purple projection on the $h - \bar{\kappa}_l$ plane in (c) and (d) is the same as in (a). A 2D plane cuts the strain data points colored in black. Solid curve segments are on d_m^{upper}. (e) $\bar{\kappa}_l$ and (f) Debye temperature θ_D vs. Ω.

A closer inspection of Figure 4d suggests that the upper boundaries of the two projections are of particular interest as they correspond to strain states which are furthest from the ESE limit at given values of $\bar{\kappa}_l$ or h. To accurately delimit these boundaries, one can adopt a similar workflow as in Eqns. (1-3) to determine the "density of states" denoted as $g(d_m)$ and then define the following upper envelope functions:

$$d_m^{\mathrm{upper}}(\bar{\kappa}_l) \equiv \sup_{d_m}\left(g(d_m; \bar{\kappa}_l)\right) \tag{7}$$

$$d_m^{\mathrm{upper}}(h) \equiv \sup_{d_m}\left(g(d_m; h)\right) \tag{8}$$

As shown in Figure 4d, $d_m^{\mathrm{upper}}(\bar{\kappa}_l)$ and $d_m^{\mathrm{upper}}(h)$ coincide with the line segments AB and CD colored in blue and green, respectively. These two envelope functions can guide deep ESE. In particular, $d_m^{\mathrm{upper}}(\bar{\kappa}_l)$ describes the path in the 6D strain space with the highest safety factor to reach a targeted $\bar{\kappa}_l$ from the undeformed state. For instance, one can apply the strains following as close as possible the curve segment AB in Figure 4d to avoid the material from going through strain states with smaller d_m values that are more likely to cause phonon instability. Note the slight difference between following $d_m^{\mathrm{upper}}(\bar{\kappa}_l)$ and following $\bar{\kappa}_l^{\mathrm{lower}}(h)$ as introduced in Figure 4a: the former is a conservative way to conduct deep ESE and always keeps a long minimum distance away from potential material failure during deformation; the latter is a more progressive way to carry out deep ESE by emphasizing energy-efficient achievement of target figure of merit of a material, regardless of how close it may get to the phonon stability boundary while undergoing deformation along the strain path in 6D. Meanwhile, the $d_m^{\mathrm{upper}}(h)$ function is useful for the optimization of strain path in 6D to achieve a deformation with certain strain energy storage. For example, to reach a target h value of 200 meV/Å^3, one can choose the states with the largest d_m value (Point D on the $d_m^{\mathrm{upper}}(h)$ envelope), and segment CD delineates a path from the undeformed state to this chosen point.

Figure 4e shows that when the volume of the crystal unit cell (Ω) decreases, the thermal conductivity of diamond generally increases. A molecular dynamics simulation qualitatively showing this trend can be found in Figure S2. When the normal deformation is compressive, decreasing Ω results in stronger covalent bonding with increased phonon frequencies ω, and greater phonon frequency dispersion. Such frequency dispersion enhancement due to reduced Ω is also reflected in the increased Debye temperature θ_D (Figure 4f and Figure S3 in Appendix). The occupancy f_0 of phonons with a greater ω would decrease according to Bose-Einstein statistics,

where $f_0 = 1/\left(e^{\frac{\hbar\omega}{k_B T}} - 1\right)$. Small wavevector phonons will therefore become more abundant than in an undeformed material at the same temperature (300 K). For a 3-phonon scattering process, the sum of two small phonon wavevectors is less likely to exceed the first Brillouin zone and satisfy momentum conservation relation $\mathbf{k} + \mathbf{k}' = \mathbf{k}'' - \mathbf{G}$. This results in fewer Umklapp and more normal phonon scattering processes, and the interaction strength of such processes $\Phi_{\lambda\lambda'\lambda''}$ (λ is shorthand for (ω, j) which represents a phonon with frequency ω and polarization j) will decrease, leading to an increase in $\bar{\kappa}_l$. For similar reasoning, a general decrease in $\bar{\kappa}_l$ can be found when the deformation is of tensile nature when 3-phonon processes with more Umklapp processes will play a major role. In this case $\Phi_{\lambda\lambda'\lambda''}$ will increase, the scattering rate $\Gamma_{\boldsymbol{\lambda}}(\omega_{\boldsymbol{\lambda}})$ will then increase, which will impede phonon propagation and shorten the phonon lifetime, $\tau_{\boldsymbol{\lambda}} = \frac{1}{2\Gamma_{\boldsymbol{\lambda}}(\omega_{\boldsymbol{\lambda}})}$.

Conclusion

First-principles calculations of the characteristics of phonons and physical properties such as thermal conductivity of semiconductors can be computationally expensive and intractable with on-the-fly computation. In this work, a unique and general approach involving neural networks is developed to capitalize on the structured and highly correlated relationship between band dispersion and strain to accurately perform a variety of tasks, including the prediction of phonon band structure and DOS. The ML models employed here are sufficiently flexible to include synergistic data sampling and active-learning cycles, which can further improve training accuracy. Direct application of this scheme to diamond crystals is demonstrated by predicting the strain hypersurface where the onset of phonon instability occurs. Employing deep ESE to modulate fundamental phonon-related properties of materials, such as thermal conductivity or phonon band structure, requires the identification of optimal actionable strain states within the 6D strain hyperspace. The example provided in this work of tuning the thermal conductivity of diamond lattice through deep ESE illustrates the opportunity for figure-of-merit optimization and customizing device performance. In particular, the prediction that the lattice thermal conductivity of diamond, nature's most thermally conductive material, can be either doubled or decreased to sub-100 $W \cdot m^{-1} \cdot K^{-1}$ values purely through elastic strain is a striking example of the application of this method. This ultra-wide dynamic range for modulating physical properties through ESE offers potential applications, as phonons control thermoelectric, superconductivity, and quantum coherence[26,27] properties as well.

Applications of such surrogate ML models are many. Just as the gradient of the electronic band relates to group velocity, the gradient of the phonon band ($\nabla_{\mathbf{k}}\omega_\nu(\mathbf{k}; \boldsymbol{\varepsilon})$) relates to the speed of sound in the medium, which could be attained by invoking this model. Other important material properties such as the Grüneisen parameter (that characterizes the effect of volume change of a crystal lattice on its vibrational properties and therefore, thermal expansion[28]) could be derived from postprocessing selected phonon band structures with certain strain states. Furthermore, various properties of a material under different strain states might be seen as competing objectives

that need to be optimized simultaneously (Pareto analysis)[6]. For example, a balance between thermal properties and electronic properties could be explored to identify the most efficient energy conversion in a thermoelectric material. Lastly, owing to its accuracy and low computational cost, it is appealing to explore adaptations of this joint ML-*ab initio* calculation framework for simulating phononic functionalities to accelerate figure-of-merit acquisition for a variety of semiconductors and to incorporate the method into technology computer-aided design (TCAD)[29–32] for industry-grade device application with deep ESE.

Method

First-principles data acquisition

Computational results for undeformed diamond were first calibrated against widely available experimental values obtained from neutron/X-ray inelastic scattering, including lattice constant, elastic properties, and phonon band structures. After the benchmark, ~15,000 Latin-Hypercube-sampled strain points were fed into ab initio calculations to acquire the phonon stability, DOS, band structures, and other related properties for each deformed structure.

For strain-deformed structure relaxation, density functional theory (DFT) simulations were carried out using the projector augmented wave method[33] with Perdew–Burke-Ernzerhof[34] exchange-correlation functional following the implementation in the Vienna Ab initio Simulation Package (VASP)[35]. For all computations, the electronic wavefunctions were expanded using a plane wave basis set characterized by an energy cutoff of 600 eV, and Brillouin zone integration was performed using a 13 × 13 × 13 Monkhorst-Pack **k**-mesh. A maximum residual force of 5.0×10^{-4}eV/Å was permitted for atoms following structural relaxation. The Green-Lagrangian strain measure was used $|\varepsilon_{ij}| \leq 0.4$ $(i, j = 1, 2, 3)$, and the strain was sampled in a sufficient range to capture the entire phonon stability boundary (main text Figure 3). Known crystal symmetries were employed to further reduce the number of strain computations needed. The diamond phonon calculations were carried out based on Γ-only density functional perturbation theory (DFPT) implemented in the VASP-Phonopy package[36,37]. The force constant calculations were conducted based on a 2 × 2 × 2 supercell of diamond and 3 × 3 × 3 **k**-point mesh. Given the coarseness of this mesh, Phonopy's "mesh sampling mode" was employed for the expansion/extrapolation of the results onto a 25 × 25 × 25 grid. ML models were then trained upon learning this dense grid of frequency eigenvalues. Phono3py package[36,37] was employed for deformed diamond lattice thermal conductivity calculations through a direct solution of the linearized phonon Boltzmann transport equation.

Model architecture

The input and output data structures of the FNN and CNN-based models used in this work are illustrated in the main text Figure 1. The FNN models reaching the best accuracies for learning phonon stability, DOS, and band structure all involve three hidden layers: 6–(256–128–64)–1, 6–(2048–2048–4096)– w, and 6–(1024–1024–2048)– $6m^3$, respectively. Here, w dictates the

resolution of the DOS plot, and m is the number of **k**-points sampled in the Brillouin zone. The CNN-based model yielding the best learning result for the band structure fitting task consists of a fully-connected part at the beginning to "unpack" the 6 × 1 vector denotation of $\boldsymbol{\varepsilon}$ into an $m \times m \times m \times 6$ tensor representation in order to be fed into the subsequent convolutional part with three blocks of convolution with a (3 × 3 × 3 × 3) kernel subsequently applied upon the floating-point representation residually. It has been demonstrated in previous works regarding electronic band structure in diamond that such convolutions account for the so-called "inter/intra-band correlations"[6] with periodic boundary conditions and symmetry. Likewise, the CNN-based model yielding the best outcomes for the DOS fitting task morphs the 6 × 1 representation of $\boldsymbol{\varepsilon}$ into a $w \times 1$ vector by a series of fully connected layers, which is treated by two blocks of 1D convolution: the first with a (7 × 1) kernel and the second with a (3 × 1) kernel. Each convolution comes with 16 channels. After that, we did channel-wise down-sampling and applied the result residually to the original $w \times 1$ vector. The Adam stochastic optimization algorithm was used to train the model, together with the gradually reducing dropout rate for fully-connected layers to enhance learning and prevent overfitting.

Molecular dynamics (MD) simulation

Thermal conductivity of diamond was computed via the equilibrium Green-Kubo formalism[38,39], a methodology that connects the ensemble average of heat flux auto-correlation to thermal conductivity. Heat flux vectors were calculated based on atomic contributions (from atomic energies, velocities, and stresses). Thermal conductivity calculations require a sufficiently large simulation box to address the large mean free path of phonons, which is critical for high lattice thermal conductivity materials such as diamond. We first tested both sample size and correlation length dependencies to ensure the convergence of the thermal conductivity calculation. The convergence was established at a correlation length of at least 30 ps and a sample size of at least 60×60×60 a_0^3, where a_0 is the equilibrium lattice constant at 300 K. For production MD runs, we first equilibrated all samples, inclusive of those exposed to varying hydrostatic strains, for 100 ps under NVT conditions. Then heat flux auto-correlation was determined over an additional 1 ns NVT MD run. The final thermal conductivity corresponding to a specific hydrostatic strain was obtained by time-averaging across the 1 ns period. All MD simulations were based on Tersoff potential obtained from the NIST repository[40] to provide qualitative trends.

Acknowledgments

The computations involved in this work were conducted on the Frontera cluster of the Texas Advanced Computing Center and the Engaging cluster at the Massachusetts Institute of Technology (MIT) Nuclear Science Engineering department. Z.S. and J.L. acknowledge support from the Defense Threat Reduction Agency under Grant No. HDTRA1-20-2-0002. E.T. worked on this project as an independent researcher. A.B. acknowledges support from a National Science Foundation Graduate Research Fellowship under Grant No. DGE-174530. W.S. acknowledges the support from the postdoctoral fellowship from the School of Biological Sciences, Nanyang

Technological University. M.D. acknowledges support from MIT J-Clinic for Machine Learning and Health. S.S. acknowledges support from MIT through the Vannevar Bush Professorship and from Nanyang Technological University through the Distinguished University Professorship.

Competing interests

The authors declare no competing interests.

References

1. Li, J., Shan, Z. & Ma, E. Elastic strain engineering for unprecedented materials properties. *MRS Bulletin* **39**, 108–114 (2014).
2. Dang, C. *et al.* Extreme mechanics of nanoscale diamond towards functional device applications. *Extreme Mechanics Letters* **58**, 101931 (2023).
3. Lu, A. *et al.* Tuning diamond electronic properties for functional device applications. *Functional Diamond* **2**, 151–165 (2022).
4. Sze, S. M. & Ng, K. K. *Physics of Semiconductor Devices*. (John Wiley & Sons, 2006).
5. Shi, Z. *et al.* Deep elastic strain engineering of bandgap through machine learning. *PNAS* **116**, 4117–4122 (2019).
6. Tsymbalov, E. *et al.* Machine learning for deep elastic strain engineering of semiconductor electronic band structure and effective mass. *npj Comput Mater* **7**, 1–10 (2021).
7. Parton, E. & Verheyen, P. Strained silicon — the key to sub-45 nm CMOS. *III-Vs Review* **19**, 28–31 (2006).
8. Sun, G., Sun, Y., Nishida, T. & Thompson, S. E. Hole mobility in silicon inversion layers: Stress and surface orientation. *Journal of Applied Physics* **102**, 084501 (2007).
9. Vogelsang, T. & Hofmann, K. R. Electron mobilities and high-field drift velocities in strained silicon on silicon-germanium substrates. *IEEE Transactions on Electron Devices* **39**, 2641–2642 (1992).

10. Liu, X., Gu, J., Shen, Y. & Li, J. Crystal metamorphosis at stress extremes: how soft phonons turn into lattice defects. *NPG Asia Materials* **8**, e320–e320 (2016).
11. Banerjee, A. *et al.* Ultralarge elastic deformation of nanoscale diamond. *Science* **360**, 300–302 (2018).
12. Nie, A. *et al.* Approaching diamond's theoretical elasticity and strength limits. *Nature Communications* **10**, 1–7 (2019).
13. Dang, C. *et al.* Achieving large uniform tensile elasticity in microfabricated diamond. *Science* **371**, 76–78 (2021).
14. Zhang, J. *et al.* Achieving 5.9% elastic strain in kilograms of metallic glasses: Nanoscopic strain engineering goes macro. *Materials Today* **37**, 18–26 (2020).
15. Zhang, H. *et al.* Approaching the ideal elastic strain limit in silicon nanowires. *Science Advances* **2**, e1501382 (2016).
16. Shi, Z. *et al.* Metallization of diamond. *PNAS* **117**, 24634–24639 (2020).
17. Li, J. EML webinar overview: Elastic Strain Engineering for unprecedented properties. *Extreme Mechanics Letters* **54**, 101430 (2022).
18. Mounet, N. & Marzari, N. First-principles determination of the structural, vibrational and thermodynamic properties of diamond, graphite, and derivatives. *Phys. Rev. B* **71**, 205214 (2005).
19. Guo, Z. *et al.* Fast and accurate machine learning prediction of phonon scattering rates and lattice thermal conductivity. *npj Comput Mater* **9**, 1–10 (2023).
20. Yang, X., Feng, T., Li, J. & Ruan, X. Evidence of fifth- and higher-order phonon scattering entropy of zone-center optical phonons. *Phys. Rev. B* **105**, 115205 (2022).

21. Bonini, N., Garg, J. & Marzari, N. Acoustic Phonon Lifetimes and Thermal Transport in Free-Standing and Strained Graphene. *Nano Lett.* **12**, 2673–2678 (2012).
22. Darolia, R. Thermal barrier coatings technology: critical review, progress update, remaining challenges and prospects. *International Materials Reviews* **58**, 315–348 (2013).
23. Miyashiro, F. *et al.* High thermal conductivity aluminum nitride ceramic substrates and packages. *IEEE Transactions on Components, Hybrids, and Manufacturing Technology* **13**, 313–319 (1990).
24. Kurokawa, Y., Utsumi, K., Takamizawa, H., Kamata, T. & Noguchi, S. A1N Substrates with High Thermal Conductivity. *IEEE Transactions on Components, Hybrids, and Manufacturing Technology* **8**, 247–252 (1985).
25. Li, R., Wang, J.-X., Lee, E. & Luo, T. Physics-informed deep learning for solving phonon Boltzmann transport equation with large temperature non-equilibrium. *npj Comput Mater* **8**, 1–10 (2022).
26. Tang, H., Barr, A. R., Wang, G., Cappellaro, P. & Li, J. First-Principles Calculation of the Temperature-Dependent Transition Energies in Spin Defects. *J. Phys. Chem. Lett.* **14**, 3266–3273 (2023).
27. Wang, G. *et al.* Characterizing temperature and strain variations with qubit ensembles for their robust coherence protection. Preprint at https://doi.org/10.48550/arXiv.2205.02790 (2022).
28. Grüneisen, E. Theorie des festen Zustandes einatomiger Elemente. *Annalen der Physik* **344**, 257–306 (1912).

29. Chang, S.-T., Wang, W.-C., Lee, C.-C. & Huang, J. A TCAD simulation study of impact of strain engineering on nanoscale strained Si NMOSFETs with a silicon–carbon alloy stressor. *Thin Solid Films* **518**, 1595–1598 (2009).
30. Lophitis, N., Arvanitopoulos, A. & Antoniou, S. P. and M. *TCAD Device Modelling and Simulation of Wide Bandgap Power Semiconductors*. *Disruptive Wide Bandgap Semiconductors, Related Technologies, and Their Applications* (IntechOpen, 2018). doi:10.5772/intechopen.76062.
31. Smith, L. TCAD Modeling of Strain-Engineered MOSFETs. *MRS Online Proceedings Library (OPL)* **913**, (2006).
32. Tiwari, R. *et al.* A 3-D TCAD Framework for NBTI, Part-II: Impact of Mechanical Strain, Quantum Effects, and FinFET Dimension Scaling. *IEEE Transactions on Electron Devices* **66**, 2093–2099 (2019).
33. Blöchl, P. E. Projector augmented-wave method. *Phys. Rev. B* **50**, 17953–17979 (1994).
34. Perdew, J. P., Burke, K. & Ernzerhof, M. Generalized Gradient Approximation Made Simple. *Phys. Rev. Lett.* **77**, 3865–3868 (1996).
35. Kresse, G. & Hafner, J. Ab initio. *Phys. Rev. B* **47**, 558–561 (1993).
36. Togo, A., Chaput, L. & Tanaka, I. Distributions of phonon lifetimes in Brillouin zones. *Physical review B* **91**, 094306 (2015).
37. Togo, A. First-principles Phonon Calculations with Phonopy and Phono3py. *J. Phys. Soc. Jpn.* **92**, 012001 (2023).
38. Kubo, R. Statistical-Mechanical Theory of Irreversible Processes. I. General Theory and Simple Applications to Magnetic and Conduction Problems. *J. Phys. Soc. Jpn.* **12**, 570–586 (1957).

39. Green, M. S. Markoff Random Processes and the Statistical Mechanics of Time-Dependent Phenomena. II. Irreversible Processes in Fluids. *The Journal of Chemical Physics* **22**, 398–413 (2004).
40. Tersoff, J. Empirical Interatomic Potential for Carbon, with Applications to Amorphous Carbon. *Phys. Rev. Lett.* **61**, 2879–2882 (1988).
41. Togo, A. & Tanaka, I. First principles phonon calculations in materials science. *Scripta Materialia* **108**, 1–5 (2015).
42. Kresse, G. & Furthmüller, J. Efficient iterative schemes for ab initio total-energy calculations using a plane-wave basis set. *Physical review B* **54**, 11169 (1996).
43. Kresse, G. & Furthmüller, J. Efficiency of ab-initio total energy calculations for metals and semiconductors using a plane-wave basis set. *Computational materials science* **6**, 15–50 (1996).

Supplementary Information for

Phonon stability boundary and deep elastic strain engineering of lattice thermal conductivity

Zhe Shi[a,*], Evgenii Tsymbalov[b,*], Wencong Shi[c], Ariel Barr[a], Qingjie Li[a], Jiangxu Li[d], Xing-Qiu Chen[d], Ming Dao[e], Subra Suresh[c,e,⊥], and Ju Li[a,e,⊥]

[a] Department of Nuclear Science and Engineering, Massachusetts Institute of Technology, Cambridge, Massachusetts 02139, USA
[b] Independent Researcher, Aachen, North Rhine-Westphalia 52070, Germany
[c] Department of Mechanical Engineering, Nanyang Technological University, Singapore 639798, Republic of Singapore
[d] Shenyang National Laboratory for Materials Science, Institute of Metal Research, Chinese Academy of Sciences, Shenyang, China
[e] Department of Materials Science and Engineering, Massachusetts Institute of Technology, Cambridge, Massachusetts 02139, USA

* These authors contributed equally to this work.
⊥To whom correspondence may be addressed. Email: ssuresh@mit.edu or liju@mit.edu.

This PDF file includes:

Supplementary text
Table S1
Figures S1 to S3
References for SI reference citations

Notation

During a general three-dimensional deformation involving three normal strains, the original point group of the diamond crystal, denoted as O_h, turns into a D_{2h} point group. The corresponding Brillouin zone would not be a regular truncated octahedron with equilateral hexagonal and square faces anymore. The center of the Brillouin zone is labeled as Γ following the tradition. In an undeformed diamond, the centers of the square and regular hexagonal surfaces on the Brillouin zone boundary both degenerate, which are referred to as *X* and *L*, respectively. For the sake of comparison and simplicity, we adhere to this convention by considering the '*X*'-type points as the centers of tetragonal surfaces and the '*L*'-type points as the centers of regular or non-regular hexagonal surfaces. Connecting the Γ point to the '*X*'-type points results in lines labeled as 'Δ'-type. Consequently, while the six '*X*'- and '*L*'-type points are no longer degenerate, they maintain the correct fractional coordinates of ⟨0.5, 0, 0.5⟩-type and ⟨0.5, 0, 0⟩-type. Moreover, the k-points situated along the Γ-'*X*' line all possess coordinates of the ⟨ζ, 0, ζ⟩-type, where $0 < \zeta < 0.5$.

Theoretical background of $\boldsymbol{\kappa}_l$

The Hamiltonian of a crystal system can be written as

$$H = \Psi_0 + T + H_2 + H_3 + \cdots \tag{9}$$

where Ψ_0 is a constant potential, T the kinetic energy of ions, and H_n the n-body crystal potentials. H_2 is the harmonic potential and does not contribute to the lattice thermal resistance. The H_3 term describes three-phonon scattering processes and is the main contribution to $\boldsymbol{\kappa}_l{}^{-1}$. In the form of second quantization, these can be expressed as [36]

$$H_2 = \sum_{\lambda} \hbar\omega_\lambda \left(\frac{1}{2} + \hat{a}_\lambda^\dagger \hat{a}_\lambda\right) \tag{10}$$

$$H_3 = \sum_{\lambda\lambda'\lambda''} \Phi_{\lambda\lambda'\lambda''} \left(\hat{a}_{-\lambda}^\dagger + \hat{a}_\lambda\right)\left(\hat{a}_{-\lambda'}^\dagger + \hat{a}_{\lambda'}\right)\left(\hat{a}_{-\lambda''}^\dagger + \hat{a}_{\lambda''}\right) \tag{11}$$

where $\lambda = (\boldsymbol{q}, j)$ represents the wave vector $\boldsymbol{q}$, and polarization j of the phonon mode, and $\hat{a}_\lambda^\dagger$ and $\hat{a}_\lambda$ are the phonon creation and annihilation operators. The interaction strength of three-phonon scattering processes is given by $\Phi_{\lambda\lambda'\lambda''}$ and is the determinative factor for the value of $\boldsymbol{\kappa}_l$. The procedures for computing $\boldsymbol{\kappa}_l$ were implemented in Phonopy and Phono3py software packages, and employed a supercell approach [36,41], with individual supercells computed using VASP [42,43]. The full form of the $\boldsymbol{\kappa}_l$ tensor can be expressed as

$$\boldsymbol{\kappa}_l = \frac{1}{NV} \sum_{\lambda} C_\lambda \tau_\lambda \boldsymbol{v}_\lambda \otimes \boldsymbol{v}_\lambda \tag{12}$$

where V is the volume of the computed unit cell, N is the number of unit cells employed, $\boldsymbol{v}_\lambda$ is the group velocity of a phonon mode with wave vector $\boldsymbol{q}$ and polarization j, and τ_λ is the lifetime of each phonon mode. The lifetime can be computed as $\tau_\lambda = \frac{1}{2}\Gamma_\lambda(\omega_\lambda)$, with $\Gamma_\lambda(\omega_\lambda)$ the phonon

linewidth or phonon "self-energy" and is proportional to $|\Phi_{-\lambda\lambda'\lambda''}|^2$. The detailed expression for $\Gamma_\lambda(\omega_\lambda)$ is in the form of the selection rule of 3-phonon process [36] and can be obtained from H_3.

Table S1. Mathematical definitions of phonon softness (s) in addition to Eqn. (4). Considerations are given based on convergence. c is a constant.

Definition	Bands involved	**k**-point involved
$\frac{\sum_{\nu,\mathbf{k}} \frac{\omega_{\nu,\mathbf{k}}^2}{\lvert\mathbf{k}\rvert^2 + c}}{\sum_{\nu,\mathbf{k}} 1}$	All	All
$\frac{\sum_{\nu=1,\mathbf{k}\neq\mathbf{0}}^{\nu=3} \frac{\omega_{\nu,\mathbf{k}}^2}{\lvert\mathbf{k}\rvert^2}}{\sum_{\nu=1,\mathbf{k}\neq\mathbf{0}}^{\nu=3} 1}$	ν = 1, 2, 3	no Γ
$\frac{\sum_{\nu,\mathbf{k}\neq\mathbf{0}} \frac{\omega_{\nu,\mathbf{k}}^2}{\lvert\mathbf{k}\rvert^2}}{\sum_{\nu,\mathbf{k}\neq\mathbf{0}} 1}$	All	no Γ
$\frac{\sum_{\nu=1,\mathbf{k}}^{\nu=3} \frac{\omega_{\nu,\mathrm{k}}^2}{\lvert\mathbf{k}\rvert^2}}{\sum_{\nu=1,\mathbf{k}}^{\nu=3} 1}$	ν = 1, 2, 3	All
$\sum_{\nu=1}^{\nu=3} \int_{\mathrm{BZ}} \omega_\nu^2 d\mathbf{k}$	ν = 1, 2, 3	All

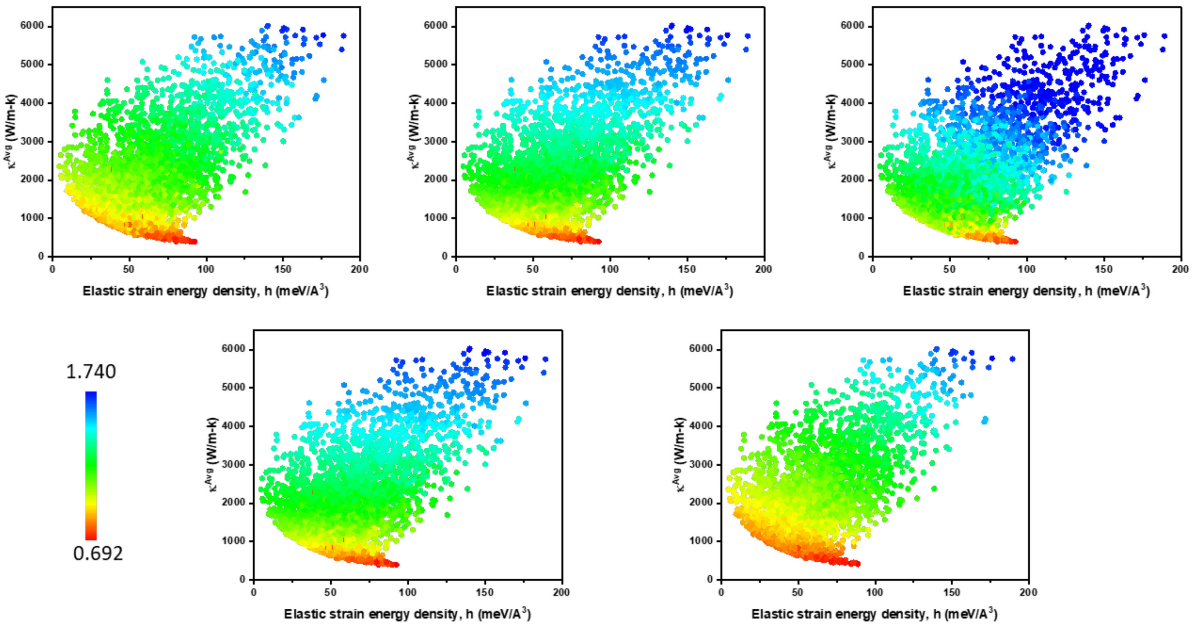

Figure S1. Thermal conductivity as a function of elastic strain energy density. The colors correspond to the relative softness derived from the definitions in Table S1.

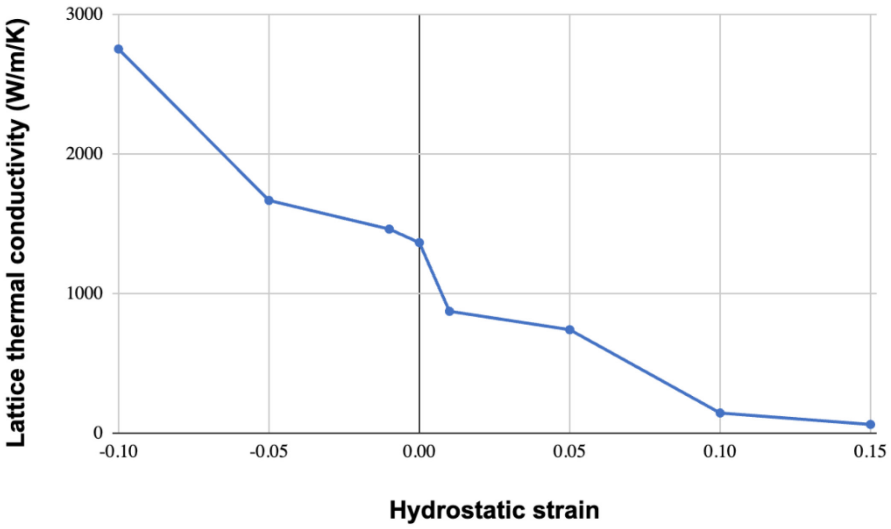

Figure S2. Alternations in the lattice thermal conductivity in response to varying hydrostatic strains by molecular dynamics (MD) simulations, utilizing a system of ~2.17 million C atoms governed by a Tersoff potential[40]. The unevenness in the curve arises from the inherent randomness of one-shot MD simulations. While the Tersoff potential itself does not explicitly model phonon interactions, the behavior that emerges from this potential can result in phonon scattering events such as 3-phonon scattering due to atomic interactions dictated by the potential. Therefore, despite the quantitative disparity in $\boldsymbol{\kappa}_l$ at a zero-strain condition, the qualitative trend of delineating the strain-dependent evolution of aligns coherently with the results in the main text.

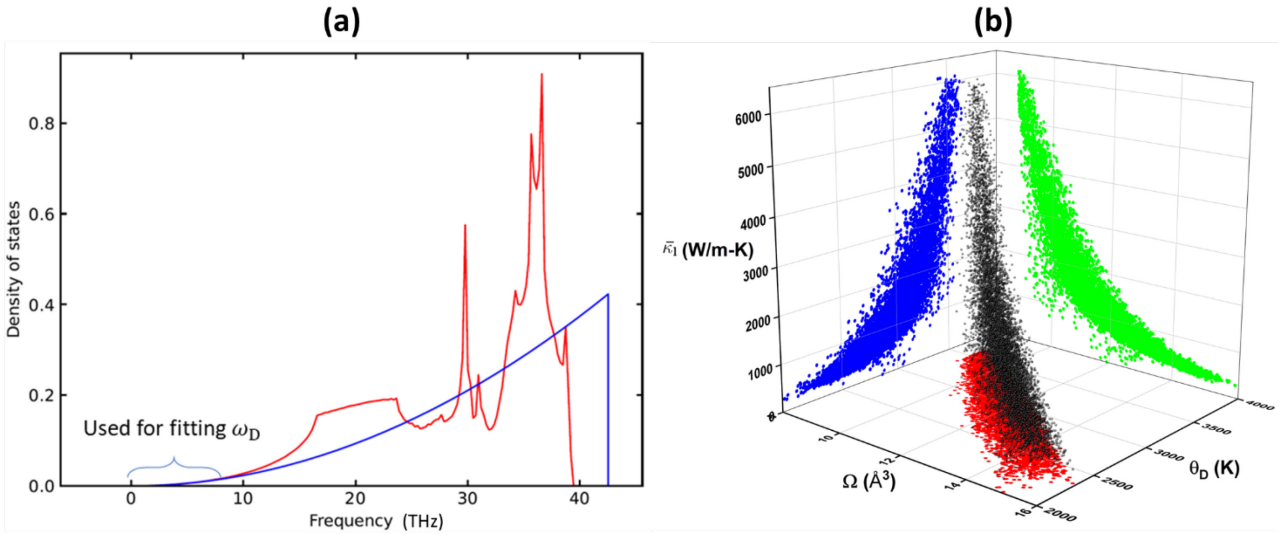

Figure S3. Debye temperature calculation and results. (a) A plot of the fitting function $\left(\frac{9N}{a}\right)^{\frac{1}{3}}$ used, where a is a fitting parameter, and ω_D is the Debye frequency. The DOS from 0 to 1/4 of the maximum phonon frequency is used for fitting, and the Debye temperature is calculated as $\theta_D = \frac{\hbar}{k_B}\omega_D$. (b) 3D scatter plot of strain distribution in the $\Omega - \theta_D - \bar{\kappa}_l$ parameter space.